GEOPHYSICS, VOL. 65, NO. 3 (MAY-JUNE 2000); P. 884–895, 17 FIGS., 3 TABLES.

Improved frequency-domain elastic wave modeling using weighted-averaging difference operators

Dong-Joo Min*, Changsoo Shin‡, Byung-Doo Kwon**, and Seunghwan Chung§

ABSTRACT

We develop a new finite-difference scheme that reduces the number of grid points per wavelength required in frequency-domain elastic modeling. Our approach computes weighted averages of the spatial second-order derivative and the mass acceleration terms using a 25-point computational stencil. By determining the weighting coefficients to minimize numerical dispersion and numerical anisotropy, we reduce the number of grid points to 3.3 per shear wavelength, with a resulting error in velocities smaller than 1%. Our choice of grid points reduces the computer memory needed to store the complex impedance matrix to 4% of that for a conventional second-order scheme and to 54% of that for a combined second-order scheme. The 25-point weighted averaging scheme of this paper makes it possible to accurately simulate realistic models. Numerical examples show that this technique can achieve the same accurate solutions with fewer grid points than those from previous frequency-domain second-order schemes. Our technique can be extended directly to 3-D elastic modeling; the computational efficiency will be even greater than that realized for 2-D models.

INTRODUCTION

Frequency-domain modeling has been developed and used successfully in forward modeling of wave propagation for the last thirty years. Frequency-domain modeling was initiated by Lysmer and Drake (1972) to account for the wave propagation in the earth and developed further by Marfurt (1984) and Marfurt and Shin (1989). Shin (1988) applied frequency-domain finite-element modeling to seismic inversion. All of these authors used the finite-element method. Pratt and Worthington (1990) and Pratt (1990a,b) have applied finite-difference modeling in the frequency domain to the inversion of crosshole tomography and seismic imaging.

The frequency-domain technique has proved to be, for viscoelastic modeling, more tractable than time-domain methods because the viscoelastic wave equation, expressed as a form of convolution integral in the time domain, is represented in linear form with a complex viscoelastic modulus. In addition, we avoid the stability limitations of time integration schemes (Marfurt, 1984). Although there is a large oscillation at the natural frequencies of a given geological model, the resonant phenomena can be prevented by adding attenuation (by introducing complex frequencies). Another advantage of the frequency-domain technique is that parallelization can be easily implemented by distributing frequencies across the computational processors. In spite of these advantages, however, the frequency-domain finite-difference modeling technique has not gained popularity because acceptable accuracy requires more grid points per wavelength than working in other domains.

To overcome this serious limitation, Jo et al. (1996) and Shin and Sohn (1998) proposed a weighted-averaging scheme for solving the 2-D scalar wave equation. Jo et al. (1996) used an optimal nine-point finite-difference operator for the approximation of a Laplacian and a mass acceleration term. To discretize the Laplacian operator, they computed a weighted average of finite-difference operators that were formulated in coordinate systems rotated at 0° and 45°. The mass acceleration term was approximated by Jo et al. (1996) by combining the lumped mass and the consistent mass matrix operators. This nine-point scheme reduces the number of grid points to 5 per wavelength, achieving errors within 1%. Shin and Sohn (1998)

Manuscript received by the Editor August 18, 1997; revised manuscript received September 1, 1999.
*KORDI, Marine Geology & Geophysics Div., Ansan P.O. Box 29, Kyungki 425-600, Korea. E-mail: djmin@kordi.re.kr.
‡Seoul National Univ., School of Civil, Urban and Geosystem Engr., San 56-1, Sinlim-dong, Kwanak-Gu, Seoul 151-742, Korea. E-mail: css@model.snu.ac.kr.
**Seoul National Univ., Dept of Earth Sciences, San 56-1, Sinlim-dong, Kwanak-Gu, Seoul 151-742, Korea. E-mail: bdkwon@mantle.snu.ac.kr.
§Korea Institute of Geology, Mining and Materials, P.O. Box 111, Taedok Science Town, Daejon 305-350, Korea. E-mail: bigchung@rock25t.kigam.re.kr.

designed a 25-point operator that approximated a Laplacian operator and a mass acceleration term by using several finite-difference operators obtained over a few sets of mesh points rotated at four different angles. The number of grid points per wavelength can be reduced to 2.5 by using a 25-point scheme, with errors no larger than 1%.

Štekl and Pratt (1998) extended the method of Jo et al. (1996) to the elastic wave equations by introducing a 45°-rotated operator within a conventional second-order scheme. Four grid points per wavelength are required for this scheme to achieve errors less than 5%. If the errors are held within 1%, Štekl and Pratt's (1998) method needs approximately 9 grid points per wavelength. To achieve this improved result, they used weighting coefficients dependent on Poisson's ratio. For a model in which Poisson's ratio varies widely, however, the weighting coefficients must be independent of Poisson's ratio. In that case, the number of grid points per wavelength required by Štekl and Pratt (1998) is larger than 4, even at 5% error. To simulate realistic models accurately, we must reduce the number of grid points per wavelength further.

In this paper, we propose a 25-point weighted-averaging scheme which, for 2-D elastic modeling in the frequency domain, is more accurate. Our method uses 25 grid points to formulate finite-difference operators for 2-D elastic wave equations, as does the method proposed by Shin and Sohn (1998) for the scalar wave equation. However, we do not rotate the coordinate system nor the mesh points. By determining weighting coefficients independent of the Poisson's ratio using a Gauss-Newton method, we obtain a 25-point scheme applicable to any inhomogeneous model.

In the following sections, we describe how to formulate finite-difference operators using the 25-point scheme. This is followed by an explanation of our method for determining the weighting coefficients. Next, we estimate the numerical errors of the 25-point scheme by analyzing dispersion relations, assess the accuracy by comparing numerical solutions with analytic solutions, and examine computational advantages by computing the storage requirements for the complex impedance matrix. Finally, we synthesize seismograms for a vertical-step model to check the validity of the 25-point scheme.

THEORY

A new finite-difference operator

In a 2-D Cartesian coordinate system with the x-axis horizontal and positive to the right and the z-axis positive downward, the frequency-domain elastic wave equations in a homogeneous medium are

$$-\rho\omega^2 u = (\lambda+2\mu)^2\frac{\partial^2 u}{\partial x^2} + \mu^2\frac{\partial^2 u}{\partial z^2} + (\lambda+\mu)\frac{\partial^2 v}{\partial x\partial z} \quad (1)$$

and

$$-\rho\omega^2 v = (\lambda+2\mu)\frac{\partial^2 v}{\partial z^2} + \mu\frac{\partial^2 v}{\partial x^2} + (\lambda+\mu)\frac{\partial^2 u}{\partial x\partial z}, \quad (2)$$

where u and v are the horizontal and vertical displacements, respectively; ω is the angular frequency; ρ is the density; and λ and μ are Lamé constants.

As a possible solution for improving the accuracy of finite-difference modeling with a larger grid interval, we extend the computational grid points used for approximation of spatial derivatives and mass acceleration terms to 25 (i.e., a 5×5 star) around the collocation point. For the approximation of the spatial derivatives, our approach is to form as many finite-difference operators as possible using 25 grid points and then to average the operators using weighting coefficients. For the mass acceleration terms, the method distributes mass acceleration at the collocation point into 25 grid points around the collocation point.

The homogeneous equations have six second-order partial derivative terms: $(\partial^2 u/\partial x^2)$, $(\partial^2 u/\partial z^2)$, $(\partial^2 u/\partial x\partial z)$, $(\partial^2 v/\partial x^2)$, $(\partial^2 v/\partial z^2)$, and $(\partial^2 v/\partial x\partial z)$. Figure 1 shows mesh points used to approximate the differential operators in the 25-point scheme. The finite-difference stencil for $(\partial^2 u/\partial x^2)$ is shown in Figure 1a. It is possible to formulate two centered finite-difference operators using five grid points in each row. One finite-difference operator consists of the first, third, and fifth nodal points in each row (unfilled circles in Figure 1a), and the other consists of the second, third, and fourth nodal points (filled circles in Figure 1a). The two possible finite-difference operators obtained in each row are averaged using the weighting coefficients c (for filled circles) and d (for unfilled circles). Five finite-difference operators, given as a result of the above process for all five rows, are then averaged using weighting coefficients b_1, b_2, and b_3. We assume that the second and the fourth row have the same weighting coefficient, b_2, and that the first and the fifth row have

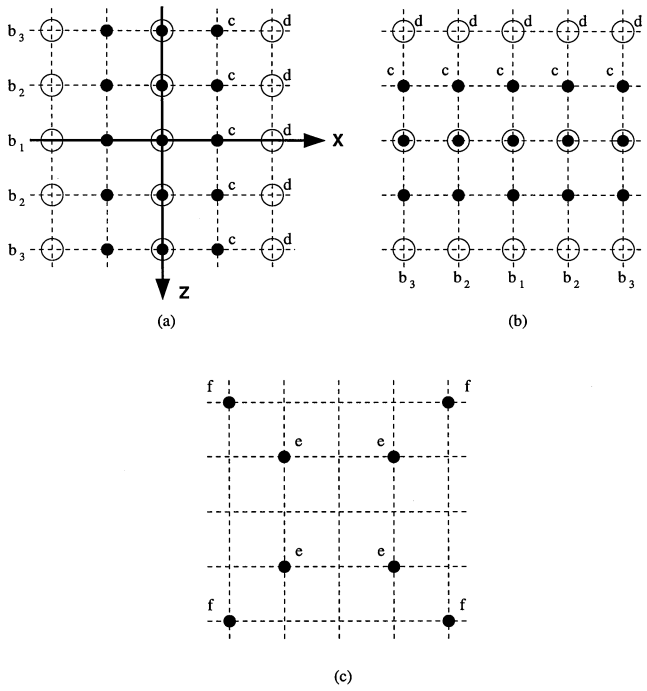

FIG. 1. Computational grids used to approximate differential operators by the 25-point weighted-averaging scheme for (a) $(\partial^2 u/\partial x^2)$, (b) $(\partial^2 u/\partial z^2)$, and (c) $(\partial^2 u/\partial x\partial z)$. The weighting coefficients c and d are used for averaging two finite-difference operators made in each row or column for approximation of $(\partial^2 u/\partial x^2)$ or $(\partial^2 u/\partial z^2)$; c is the averaging coefficient for filled circles, and d for unfilled circles. The coefficients b_1, b_2, and b_3 are used for averaging five finite-difference operators resulting from averaging two finite-difference operators with c and d in each row or column for approximation of $(\partial^2 u/\partial x^2)$ or $(\partial^2 u/\partial z^2)$. The coefficients e and f are used for averaging two finite-difference operators for $(\partial^2 u/\partial x\partial z)$.

the same weighting coefficient, b_3. A similar method is applied to the approximation of $(\partial^2 u/\partial z^2)$ (see Figure 1b). The mesh points for the approximation of $(\partial^2 u/\partial x \partial z)$ are shown in Figure 1c. Two finite-difference operators can be formulated, as shown in Figure 1c. Averaging the finite-difference operators with weighting coefficients e and f results in the expression of discretization for $(\partial^2 u/\partial x \partial z)$.

The full set of finite-difference formulae for $(\partial^2 u/\partial x^2)$, $(\partial^2 u/\partial z^2)$, and $(\partial^2 u/\partial x \partial z)$ in the 25-point scheme is

$$\begin{aligned}
\frac{\partial^2 u}{\partial x^2} \approx\ & \frac{b_1}{\Delta x^2}\Big[c(u_{i+1,j} - 2u_{i,j} + u_{i-1,j}) \\
& + \frac{d}{4}(u_{i+2,j} - 2u_{i,j} + u_{i-2,j})\Big] \\
& + \frac{b_2}{\Delta x^2}\Big[c(u_{i+1,j+1} - 2u_{i,j+1} + u_{i-1,j+1}) \\
& + \frac{d}{4}(u_{i+2,j+1} - 2u_{i,j+1} + u_{i-2,j+1})\Big] \\
& + \frac{b_2}{\Delta x^2}\Big[c(u_{i+1,j-1} - 2u_{i,j-1} + u_{i-1,j-1}) \\
& + \frac{d}{4}(u_{i+2,j-1} - 2u_{i,j-1} + u_{i-2,j-1})\Big] \\
& + \frac{b_3}{\Delta x^2}\Big[c(u_{i+1,j+2} - 2u_{i,j+2} + u_{i-1,j+2}) \\
& + \frac{d}{4}(u_{i+2,j+2} - 2u_{i,j+2} + u_{i-2,j+2})\Big] \\
& + \frac{b_3}{\Delta x^2}\Big[c(u_{i+1,j-2} - 2u_{i,j-2} + u_{i-1,j-2}) \\
& + \frac{d}{4}(u_{i+2,j-2} - 2u_{i,j-2} + u_{i-2,j-2})\Big], \qquad (3) \\
\frac{\partial^2 u}{\partial z^2} \approx\ & \frac{b_1}{\Delta z^2}\Big[c(u_{i,j+1} - 2u_{i,j} + u_{i,j-1}) \\
& + \frac{d}{4}(u_{i,j+2} - 2u_{i,j} + u_{i,j-2})\Big] \\
& + \frac{b_2}{\Delta z^2}\Big[c(u_{i+1,j+1} - 2u_{i+1,j} + u_{i+1,j-1}) \\
& + \frac{d}{4}(u_{i+1,j+2} - 2u_{i+1,j} + u_{i+1,j-2})\Big] \\
& + \frac{b_2}{\Delta z^2}\Big[c(u_{i-1,j+1} - 2u_{i-1,j} + u_{i-1,j-1}) \\
& + \frac{d}{4}(u_{i-1,j+2} - 2u_{i-1,j} + u_{i-1,j-2})\Big] \\
& + \frac{b_3}{\Delta z^2}\Big[c(u_{i+2,j+1} - 2u_{i+2,j} + u_{i+2,j-1}) \\
& + \frac{d}{4}(u_{i+2,j+2} - 2u_{i+2,j} + u_{i+2,j-2})\Big] \\
& + \frac{b_3}{\Delta z^2}\Big[c(u_{i-2,j+1} - 2u_{i-2,j} + u_{i-2,j-1}) \\
& + \frac{d}{4}(u_{i-2,j+2} - 2u_{i-2,j} + u_{i-2,j-2})\Big], \qquad (4)
\end{aligned}$$

and

$$\begin{aligned}
\frac{\partial^2 u}{\partial x \partial z} \approx\ & \frac{e}{4\Delta x \Delta z} \\
& \times [u_{i+1,j+1} - u_{i+1,j-1} - u_{i-1,j+1} + u_{i-1,j-1}] \\
& + \frac{f}{16\Delta x \Delta z} \\
& \times [u_{i+2,j+2} - u_{i+2,j-2} - u_{i-2,j+2} + u_{i-2,j-2}]. \qquad (5)
\end{aligned}$$

Finite-difference operators of $(\partial^2 v/\partial x^2)$, $(\partial^2 v/\partial z^2)$, and $(\partial^2 v/\partial x \partial z)$ are formed in the same way.

The elastic wave equations also have two mass acceleration terms; $\rho\omega^2 u$ and $\rho\omega^2 v$. To approximate the mass acceleration terms, we use the method of Shin and Sohn (1998). A mass acceleration operator is distributed over all 25 points (including the collocation); that is, the mass accelerations of 25 grid points are averaged with weighting coefficients $a_1, a_2, \ldots, a_6$. Figure 2 shows the mesh points used for the approximation of the mass acceleration term. The same weighting coefficients are given to the nodes that have the same distance from the collocation, as those shown in Figure 2. The finite-difference operator of $\rho\omega^2 u$ can be expressed as

$$\begin{aligned}
\rho\omega^2 u \approx\ & \rho\omega^2 a_1 u_{i,j} + \rho\omega^2 a_2(u_{i,j+1} + u_{i+1,j} + u_{i,j-1} + u_{i-1,j}) \\
& + \rho\omega^2 a_3(u_{i+1,j+1} + u_{i+1,j-1} + u_{i-1,j-1} + u_{i-1,j+1}) \\
& + \rho\omega^2 a_4(u_{i,j+2} + u_{i+2,j} + u_{i,j-2} + u_{i-2,j}) \\
& + \rho\omega^2 a_5(u_{i+2,j+1} + u_{i+2,j-1} + u_{i+1,j-2} + u_{i-1,j-2} \\
& + u_{i-2,j-1} + u_{i-2,j+1} + u_{i-1,j+2} + u_{i+1,j+2}) \\
& + \rho\omega^2 a_6(u_{i+2,j+2} + u_{i+2,j-2} \\
& + u_{i-2,j-2} + u_{i-2,j+2}); \qquad (6)
\end{aligned}$$

$\rho\omega^2 v$ can be written in the same form.

We can also formulate finite-difference operators for heterogeneous media, where density and elastic constants vary spatially. We combine the above approach for homogeneous

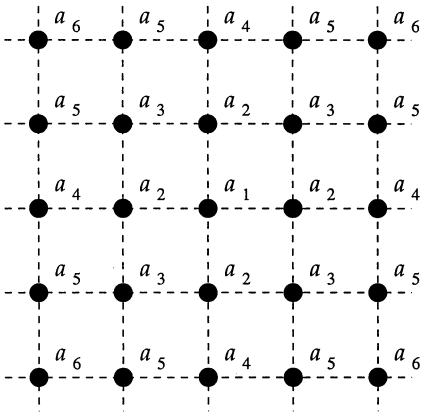

FIG. 2. Computational grids used to approximate the mass acceleration terms by the 25-point weighted-averaging scheme. The weighting coefficients $a_1, a_2, \ldots, a_6$ are used for averaging 25 grid points.

media with the heterogeneous formulation suggested by Kelly et al. (1976).

Determination of weighting coefficients

To minimize grid dispersion and numerical anisotropy, we must determine the weighting coefficients that make normalized phase and group velocities close to unity. The normalized phase and group velocities are obtained from dispersion relations.

We assume a uniform and infinite medium that supports a plane wave, expressed as $\mathbf{u}_\omega(x,z)=(u_\omega, v_\omega)e^{i(k_x x+k_z z)}$, in the frequency domain. Finite-difference approximations for the homogeneous elastic wave equations in matrix form are

$$\begin{bmatrix} \omega^2 D_m + \left(\alpha^2 D_{xx} + \beta^2 D_{zz}\right) & (\alpha^2-\beta^2)D_{xz} \\ (\alpha^2-\beta^2)D_{xz} & \omega^2 D_m + \left(\beta^2 D_{xx} + \alpha^2 D_{zz}\right) \end{bmatrix} \mathbf{u}_\omega = \mathbf{0}, \tag{7}$$

where D_{xx}, D_{xz}, and D_{zz} are the finite-difference operators for spatial derivatives; D_m is the mass acceleration operator; and α and β are the compressional- and shear-wave velocities. Under the condition that the determinant of the matrix is zero, we obtain the dispersion relations

$$\omega^2 = \frac{1}{2D_m}\Big[(\alpha^2+\beta^2)(-D_{xx}-D_{zz}) \pm (\alpha^2-\beta^2)\sqrt{(D_{xx}-D_{zz})^2+4D_{xz}^2}\Big], \tag{8}$$

where the two signs give the compressional- and the shear-wave dispersion relation, respectively. Substituting the finite-difference operators formulated by the 25-point scheme and the plane-wave solution into equation (8) yields

$$\omega^2 = \frac{1}{2\Delta^2 A}\Big[(\alpha^2+\beta^2)B \pm (\alpha^2-\beta^2)\sqrt{C}\Big], \tag{9}$$

where A, B, and C are

$$A = P_m, \tag{10}$$

$$B = -P_{xx} - P_{zz}, \tag{11}$$

and

$$C = (P_{xx}-P_{zz})^2 + 4P_{xz}^2. \tag{12}$$

for these equations,

$$\begin{aligned} P_m = {} & a_1 + 2a_2[\cos(k_x\Delta)+\cos(k_z\Delta)] \\ & + 4a_3\cos(k_x\Delta)\cos(k_z\Delta) \\ & + 2a_4[\cos(2k_x\Delta)+\cos(2k_z\Delta)] \\ & + 4a_5[\cos(2k_x\Delta)\cos(k_z\Delta) \\ & + \cos(k_x\Delta)\cos(2k_z\Delta)] \\ & + 4a_6\cos(2k_x\Delta)\cos(2k_z\Delta), \end{aligned} \tag{13}$$

$$P_{xx} = -\left[4c\sin^2\frac{k_x\Delta}{2} + d\sin^2(k_x\Delta)\right] \times [b_1 + 2b_2\cos(k_z\Delta) + 2b_3\cos(2k_z\Delta)], \tag{14}$$

$$P_{zz} = -\left[4c\sin^2\frac{k_z\Delta}{2} + d\sin^2(k_z\Delta)\right] \times [b_1 + 2b_2\cos(k_x\Delta) + 2b_3\cos(2k_x\Delta)], \tag{15}$$

and

$$P_{xz} = -e\sin(k_x\Delta)\sin(k_z\Delta) - \frac{f}{4}\sin(2k_x\Delta)\sin(2k_z\Delta) \tag{16}$$

for the special case of

$$\Delta = \Delta x = \Delta z.$$

Note that A, B, and C are functions of the weighting coefficients, grid interval, and horizontal and vertical wavenumbers. The horizontal and vertical wavenumbers, i.e., k_x ($=k_p\cos\theta$ or $k_s\cos\theta$) and k_z ($=k_p\sin\theta$ or $k_s\sin\theta$), are functions of the propagation angle, θ, with respect to the x-axis. The phase velocities are defined as

$$\alpha_{ph} = \frac{\omega}{k_p} \tag{17}$$

and

$$\beta_{ph} = \frac{\omega}{k_s} \tag{18}$$

for compressional and shear waves, respectively. Substituting equation (9) into equations (17) and (18) yields the normalized phase velocities for compressional and shear waves:

$$\frac{\alpha_{ph}}{\alpha} = \frac{1}{2\pi\dfrac{\beta}{\alpha}\dfrac{1}{G_s}}\left\{\frac{1}{2A}\left[\left(1+\frac{\beta^2}{\alpha^2}\right)B + \left(1-\frac{\beta^2}{\alpha^2}\right)\sqrt{C}\right]\right\}^{\frac{1}{2}} \tag{19}$$

and

$$\frac{\beta_{ph}}{\beta} = \frac{1}{2\pi\dfrac{1}{G_s}}\left\{\frac{1}{2A}\left[\left(1+\frac{\alpha^2}{\beta^2}\right)B + \left(1-\frac{\alpha^2}{\beta^2}\right)\sqrt{C}\right]\right\}^{\frac{1}{2}}, \tag{20}$$

where G_s is the number of nodal points per shear wavelength.

One of the most effective methods that can be used to determine the weighting coefficients is the Gauss-Newton method (Lines and Treitel, 1984). When using the Gauss-Newton method, we do not need any constraints, unlike the method used by Jo et al. (1996), Shin and Sohn (1998), and Štekl and Pratt (1998). In the Gauss-Newton method, we search for the weighting coefficients that make the numerical phase velocities as close as possible to the true velocities. Since the weighting coefficients which give the best phase velocities also lead to the best group velocities, we will consider only the phase velocities to determine the optimal weighting coefficients. We will then check the errors on our group velocities. For each normalized

phase velocity resulting from a variety of Poisson's ratios, propagation angles, and grid intervals, we can define the prediction error, $e_i = d_i - F_i(\mathbf{m}), i = 1, \ldots, N$, where d_i is unity, $\mathbf{m}$ is a set of M weighting coefficients, and $F_i(\mathbf{m})$ is normalized phase velocities of compressional and shear waves. Since $F_i(\mathbf{m})$ is functions of weighting coefficients, grid interval, Poisson's ratio, and propagation angle, N is dependent upon the range and the interval length of Poisson's ratio, propagation angle, and number of grid points per wavelength used for determining the weighting coefficients. The weighting coefficients that we want to obtain should lead to the smallest overall error E, defined as

$$E = \mathbf{e}^{\mathbf{T}}\mathbf{e}, \tag{21}$$

where $\mathbf{e}$ is the error vector.

We begin with an initial guess of the weighting coefficients, $\mathbf{m}^\circ$. By supposing that the model response (normalized phase velocity) F_i is a linear function around $\mathbf{m}^\circ$, we express a small perturbation of the model response about $\mathbf{m}^\circ$ using Taylor series expansion:

$$\mathbf{F}(\mathbf{m}) = \mathbf{F}(\mathbf{m}^\circ) + \sum_{j=1}^{M} \left.\frac{\partial \mathbf{F}}{\partial m_j}\right|_{\mathbf{m}=\mathbf{m}^\circ} \left(m_j - m_j^\circ\right) \tag{22}$$

or, in matrix notation,

$$\mathbf{F}(\mathbf{m}) = \mathbf{F}(\mathbf{m}^\circ) + \mathbf{J}\Delta\mathbf{m}, \tag{23}$$

where $\mathbf{F}$ is the vector with components F_i and $\mathbf{J}$ is the Jacobian matrix $[J_{ij} = (\partial F_i/\partial m_j)]$. Then the error vector $\mathbf{e}$ is written as

$$\begin{aligned}\mathbf{e} &= \mathbf{d} - \mathbf{F}(\mathbf{m}) \\ &= \mathbf{d} - \mathbf{F}(\mathbf{m}^\circ) - \mathbf{J}\Delta\mathbf{m},\end{aligned} \tag{24}$$

where $\mathbf{d}$ is the vector with components d_i, and $\Delta\mathbf{m}$ is chosen to minimize the total error E, that is, to satisfy $(\partial E/\partial \mathbf{m}) = 0$. Then $\Delta\mathbf{m}$ is expressed by

$$\Delta\mathbf{m} = (\mathbf{J}^{\mathbf{T}}\mathbf{J})^{-1}\mathbf{J}^{\mathbf{T}}(\mathbf{d} - \mathbf{F}(\mathbf{m}^\circ)) \tag{25}$$

and a new set of weighting coefficients $\mathbf{m}$ is given as

$$\mathbf{m} = \mathbf{m}^\circ + \Delta\mathbf{m}. \tag{26}$$

In an iterative manner, we determine the optimal weighting coefficients.

We can construct the matrix $\mathbf{J}$ by changing Poisson's ratio σ, propagation angle θ, and number of grid points G_s. We change σ and $1/G_s$ from 0.01 to 0.33 in steps of 0.01, and we change θ from 0° to 45° in 15° steps. The matrix $\mathbf{J}$ becomes an overdetermined matrix whose size is 8712×13 ($8712 = 2 \times 33 \times 4 \times 33$, and 13 is the number of weighting coefficients), when both compressional and shear phase velocities are considered. In our experience, the process does not necessarily benefit from using a wider range of σ and $1/G_s$. Although we use σ up to 0.33, we also obtain good results for $\sigma = 0.4$ (see Figures 6 and 10).

The initial guess of the weighting coefficients we used in the Gauss-Newton method was

$$\begin{aligned}&a_1 = 0.39, \quad a_2 = 0.11, \quad a_3 = 0.01, \quad a_4 = 0.0, \\ &a_5 = 0.01, \quad a_6 = 0.0, \quad b_1 = 0.62, \quad b_2 = 0.18, \\ &b_3 = -0.001, \quad c = 0.685, \quad d = 0.4, \quad e = 0.95, \\ &f = 0.05.\end{aligned} \tag{27}$$

These initial values were obtained by arbitrarily changing the weighting coefficients from 0 to 1 and then by choosing the optimal values which give the minimum error of phase velocities.

The optimal set of weighting coefficients determined by the Gauss-Newton method was

$$\begin{aligned}&a_1 = 0.5128838, \quad a_2 = 0.1451598, \quad a_3 = 0.021430882, \\ &a_4 = 0.0050698, \quad a_5 = -0.0029849, \quad a_6 = 0.000114596, \\ &b_1 = 0.608781, \quad b_2 = 0.2708982, \quad b_3 = -0.025726564, \\ &c = 0.7596838, \quad d = 0.311686, \quad e = 1.204687, \\ &f = -0.026533956.\end{aligned} \tag{28}$$

The set of weighting coefficients of equation (28) is nearly independent of the physical properties of the models because we chose the weighting coefficients by taking all ranges of propagation angle and nearly a full range of Poisson's ratio into consideration. Once we determine the weighting coefficients, we can apply them to any model. The same weighting coefficients can also be used for the heterogeneous formulation.

Dispersion analysis

Given the optimal weighting coefficients, we now examine the dispersion relations by plotting phase and group velocities for different propagation angles with respect to the grid and for different values of Poisson's ratio. The compressional- and shear-wave phase velocities are obtained from equations (19) and (20).

Figures 3 and 4 depict phase velocities for compressional and shear waves obtained using the conventional scheme for Poisson's ratios of 0.25 and 0.4, respectively. From Figures 3 and 4, we see that the compressional-wave phase velocity is very dispersive and that the dispersion is isotropic. The numerical, compressional waves travel at the same phase velocity, regardless of propagation direction. On the other hand, the shear-wave phase velocities are numerically very dispersive and anisotropic. The shear-wave phase velocities are dependent on the propagation angles. Phase velocities for the 25-point scheme are shown in Figures 5 and 6. The 25-point scheme gives nearly ideal results for compressional waves, even for a large Poisson's ratio. The numerical anisotropy for shear waves is greatly reduced.

Group velocities for compressional and shear waves can be obtained by calculating $(d\omega/dk)$ from equation (9). Figures 7 and 8 show group velocities computed by the conventional scheme and Figures 9 and 10 by the 25-point scheme. Group velocities are more dispersive than phase velocities. The 25-point scheme gives nearly perfect group velocities for the compressional waves. From Figures 9 and 10, we conclude that grid dispersion and grid anisotropy from the 25-point scheme are only very weakly dependent on Poisson's ratio, and that the grid dispersion is strongest for waves traveling along the x-axis and weakest for waves traveling in the direction 30° with respect to the x-axis.

To keep the errors of group velocities within 1%, the conventional and 25-point schemes require 33.3 and 3.3 grid points per shear wavelength, respectively. The scheme introduced by Štekl and Pratt (1998) requires 9 grid points per shear wavelength to achieve the same accuracy. Our scheme thus

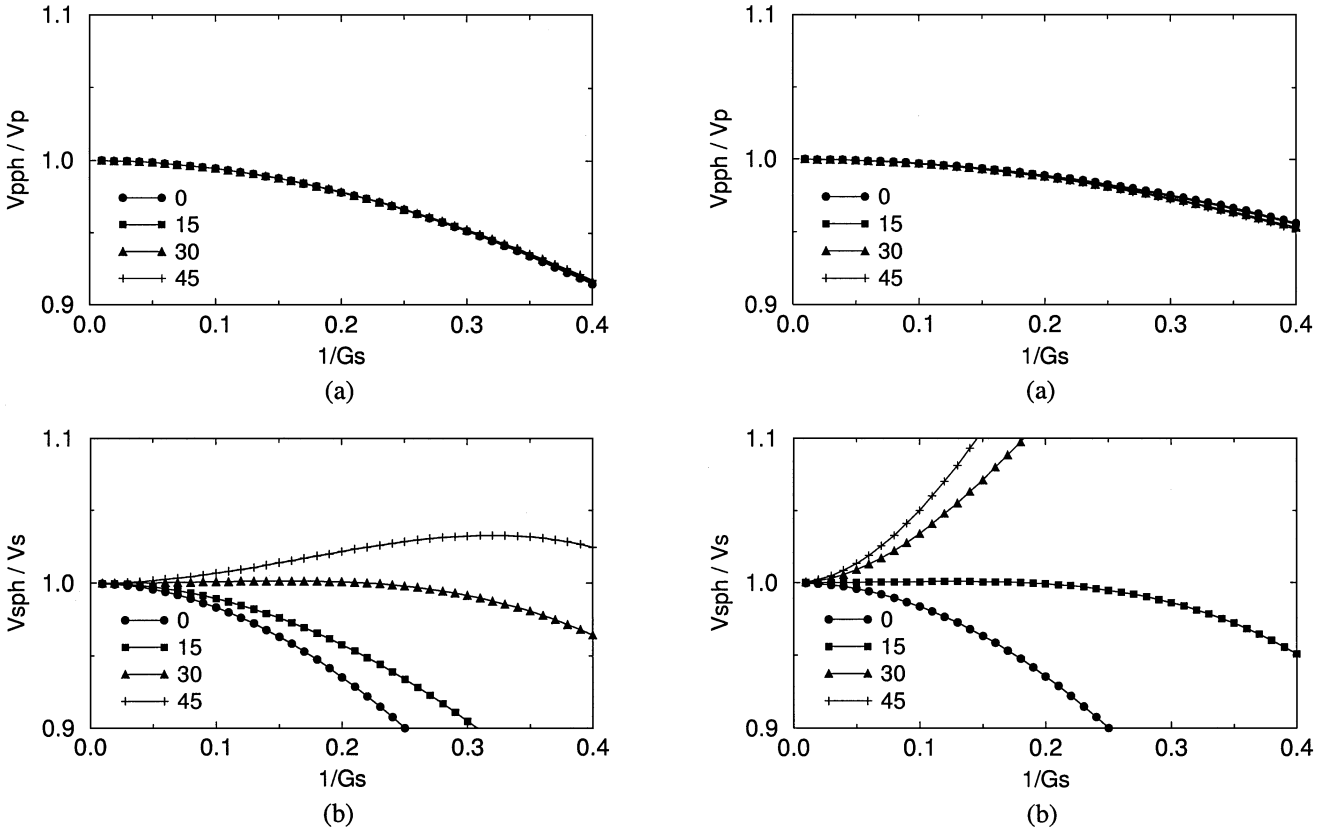

FIGS. 3, 4. Normalized phase velocities for (a) compressional waves and (b) shear waves obtained by the conventional finite-difference scheme for a Poisson's ratio of 0.25 (Figure 3, left) and 0.4 (Figure 4, right). G_s is the number of grid points per shear wavelength. Dispersion curves are plotted for propagation angles of 0°, 15°, 30°, and 45° with respect to the x-axis.

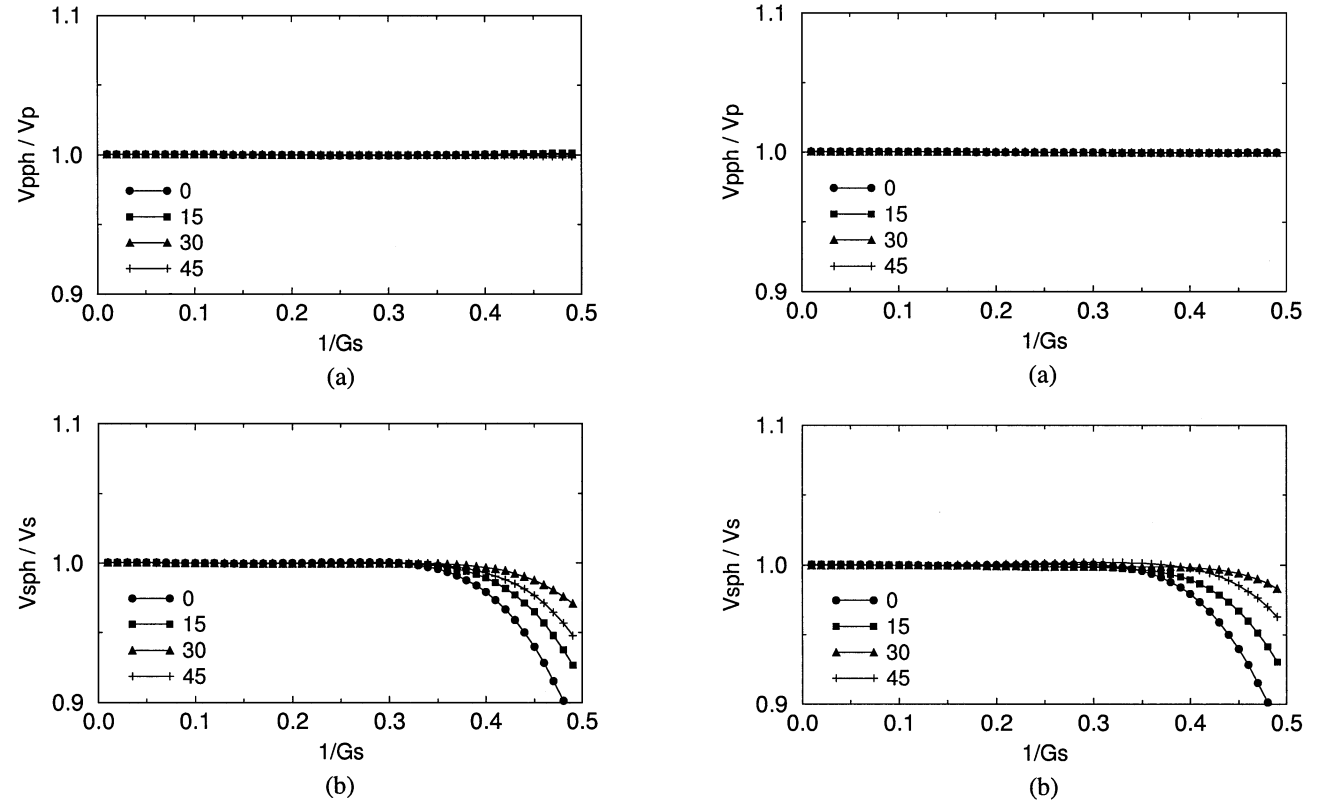

FIGS. 5, 6. Normalized phase velocities for (a) compressional waves and (b) shear waves obtained by the 25-point weighted-averaging scheme for a Poisson's ratio of 0.25 (Figure 5, left) and 0.4 (Figure 6, right). G_s is the number of grid points per shear wavelength. Dispersion curves are plotted for propagation angles of 0°, 15°, 30°, and 45° with respect to the x-axis.

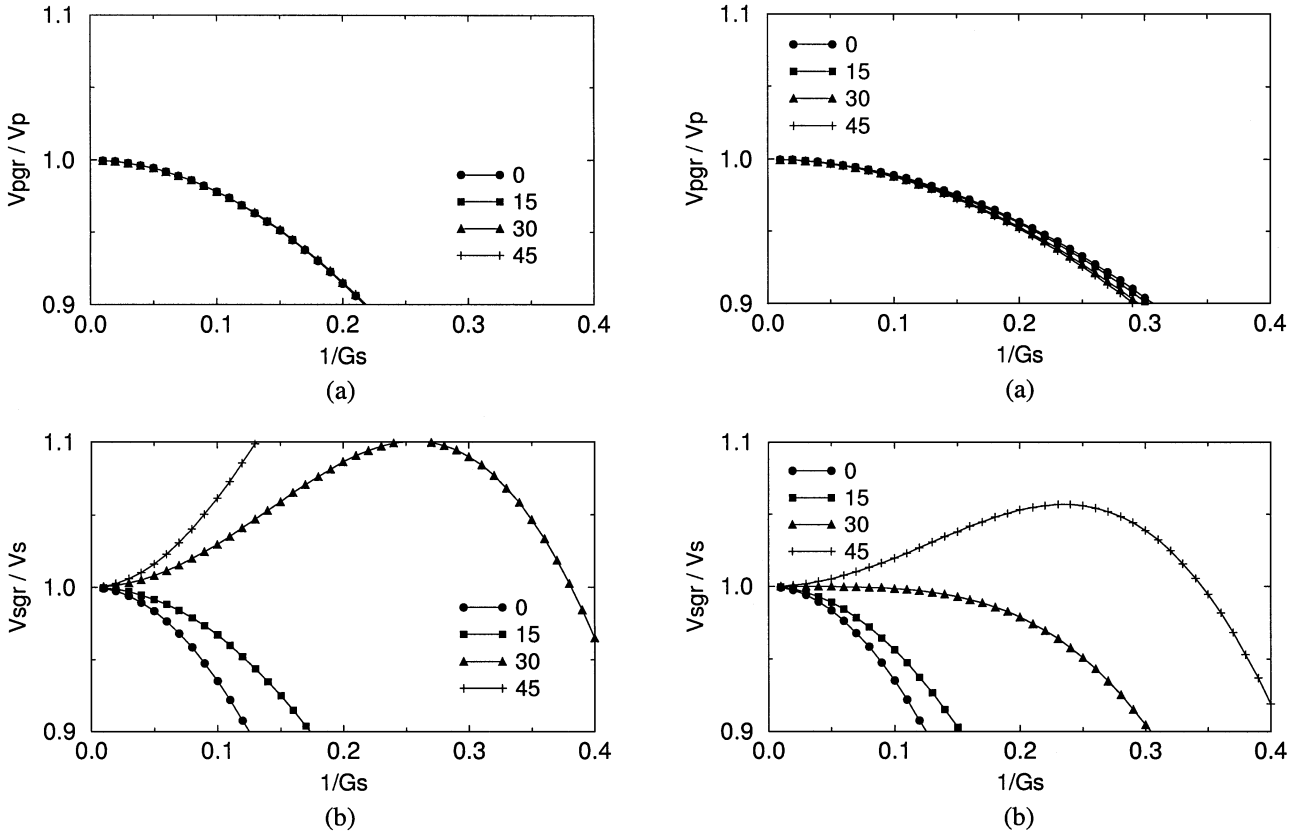

FIGS. 7, 8. Normalized group velocities for (a) compressional waves and (b) shear waves obtained by the conventional finite-difference scheme for a Poisson's ratio of 0.25 (Figure 7, left) and 0.4 (Figure 8, right). G_s is the number of grid points per shear wavelength. Dispersion curves are plotted for propagation angles of 0°, 15°, 30°, and 45° with respect to the x-axis.

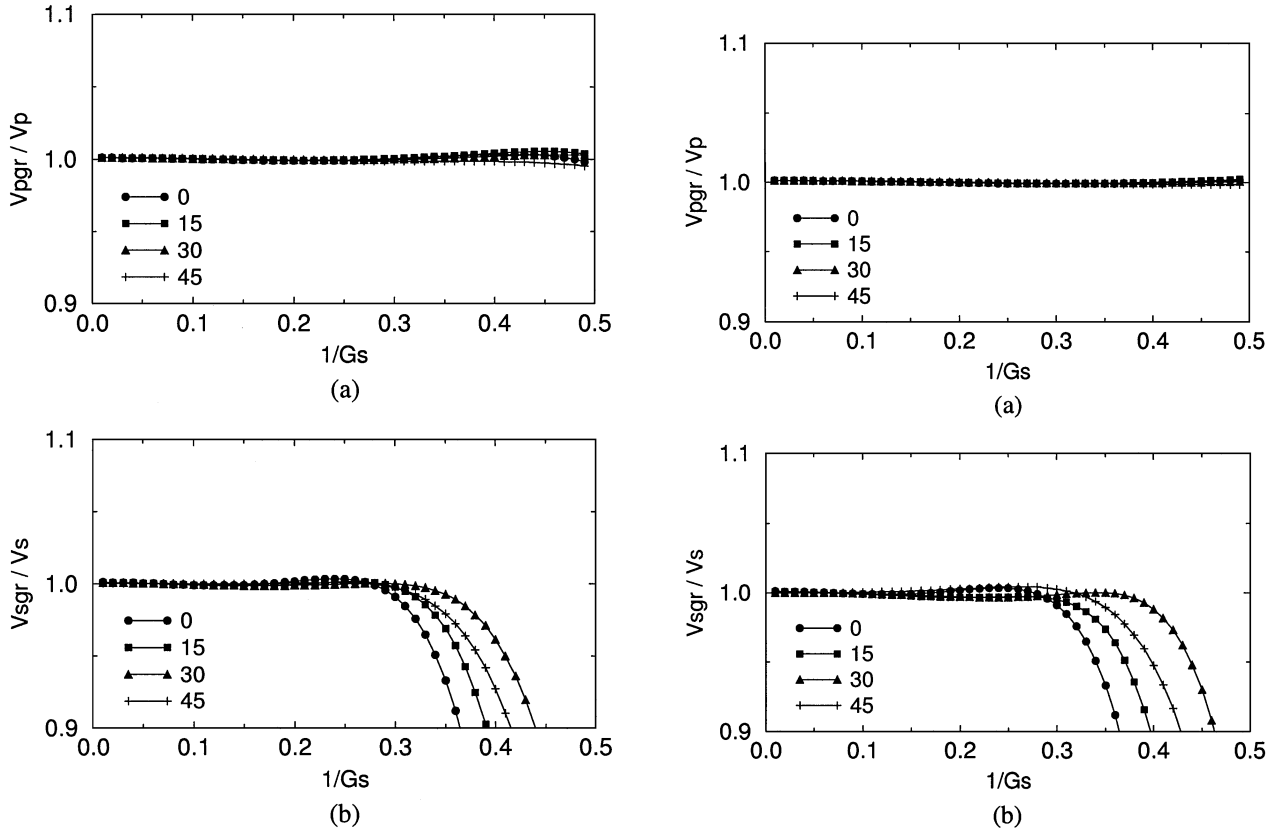

FIGS. 9, 10. Normalized group velocities for (a) compressional waves and (b) shear waves obtained by the 25-point weighted-averaging scheme for a Poisson's ratio of 0.25 (Figure 9, left) and 0.4 (Figure 10, right). G_s is the number of grid points per shear wavelength. Dispersion curves are plotted for propagation angles of 0°, 15°, 30°, and 45° with respect to the x-axis.

represents a further reduction in the number of grid points per wavelength by more than 60%.

Accuracy analysis

We use a homogeneous model for our comparison of analytic and numerical solutions. Analytic solutions of 2-D elastic wave equations for the homogeneous model are presented by Eason et al. (1956) and Pilant (1979). We obtained analytic solutions with a method similar to that used by Pilant (1979), who solved the problem by defining a scalar and a vector potential in the frequency-space domain and by using Laplace and Fourier transforms. We also applied the definition of the scalar and the vector potential in the frequency-space domain but only used the Fourier transform.

The analytic solutions in the time domain given by Pilant (1979) when a vertical source is applied in a homogeneous medium are

$$u(x,z,t) = \frac{\cos\theta\sin\theta}{2\pi\rho v_p^2}\frac{\mathrm{H}\left(t-\frac{r}{v_p}\right)}{\sqrt{t^2-\frac{r^2}{v_p^2}}} - \frac{\cos\theta\sin\theta}{2\pi\rho v_s^2}\frac{\mathrm{H}\left(t-\frac{r}{v_s}\right)}{\sqrt{t^2-\frac{r^2}{v_s^2}}} + \frac{\cos\theta\sin\theta}{\pi\rho r^2}\sqrt{t^2-\frac{r^2}{v_p^2}}\mathrm{H}\left(t-\frac{r}{v_p}\right) - \frac{\cos\theta\sin\theta}{\pi\rho r^2}\sqrt{t^2-\frac{r^2}{v_s^2}}\mathrm{H}\left(t-\frac{r}{v_s}\right) \quad (29)$$

and

$$v(x,z,t) = \frac{\cos^2\theta}{2\pi\rho v_p^2}\frac{\mathrm{H}\left(t-\frac{r}{v_p}\right)}{\sqrt{t^2-\frac{r^2}{v_p^2}}} + \frac{\sin^2\theta}{2\pi\rho v_s^2}\frac{\mathrm{H}\left(t-\frac{r}{v_s}\right)}{\sqrt{t^2-\frac{r^2}{v_s^2}}} + \frac{\cos^2\theta-\sin^2\theta}{2\pi\rho r^2}\sqrt{t^2-\frac{r^2}{v_p^2}}\mathrm{H}\left(t-\frac{r}{v_p}\right) + \frac{\sin^2\theta-\cos^2\theta}{2\pi\rho r^2}\sqrt{t^2-\frac{r^2}{v_s^2}}\mathrm{H}\left(t-\frac{r}{v_s}\right), \quad (30)$$

with

$$\mathrm{H}\left(t-\frac{r}{v}\right) = \begin{cases} 1, & t \ge \frac{r}{v}, \\ 0, & t < \frac{r}{v}, \end{cases} \quad (31)$$

$$r = \sqrt{x^2+z^2}, \quad (32)$$

and

$$\theta = \tan^{-1}\frac{x}{z}, \quad (33)$$

where u and v are the horizontal and vertical displacements, ρ is the density, and v_p and v_s are the compressional- and shear-wave velocities. The analytic solutions of equations (29) and (30) in the time domain have singularities at $t=(r/v_p)$ and $t=(r/v_s)$. For this reason, we are unable to obtain an exact solution in the time domain. To circumvent this problem, we calculated analytic solutions in the frequency domain and took their inverse Fourier transform. The analytic solutions for a homogeneous medium in the frequency domain are

$$u(x,z,\omega) = \frac{i}{4\rho v_p^2}\cos\theta\sin\theta\mathrm{H}_0^{(1)}\left(\frac{\omega}{v_p}r\right) - \frac{i}{4\rho v_s^2}\cos\theta\sin\theta\mathrm{H}_0^{(1)}\left(\frac{\omega}{v_s}r\right) - \frac{i}{2\rho v_p}\frac{\cos\theta\sin\theta}{r\omega}\mathrm{H}_1^{(1)}\left(\frac{\omega}{v_p}r\right) + \frac{i}{2\rho v_s}\frac{\cos\theta\sin\theta}{r\omega}\mathrm{H}_1^{(1)}\left(\frac{\omega}{v_s}r\right) \quad (34)$$

and

$$v(x,z,\omega) = \frac{i}{4\rho v_p^2}\cos^2\theta\mathrm{H}_0^{(1)}\left(\frac{\omega}{v_p}r\right) + \frac{i}{4\rho v_s^2}\sin^2\theta\mathrm{H}_0\left(\frac{\omega}{v_s}r\right) - \frac{i}{4\rho v_p}\frac{\cos^2\theta-\sin^2\theta}{r\omega}\mathrm{H}_1^{(1)}\left(\frac{\omega}{v_p}r\right) - \frac{i}{4\rho v_s}\frac{\sin^2\theta-\cos^2\theta}{r\omega}\mathrm{H}_1^{(1)}\left(\frac{\omega}{v_s}r\right), \quad (35)$$

with

$$i=\sqrt{-1},$$

where ω is the angular frequency, $\mathrm{H}_0^{(1)}[(\omega/v_p)r]$ and $\mathrm{H}_0^{(1)}[(\omega/v_s)r]$ are Hankel functions of the first kind of zero order, and $\mathrm{H}_1^{(1)}[(\omega/v_p)r]$ and $\mathrm{H}_1^{(1)}[(\omega/v_s)r]$ are Hankel functions of the first kind of the first order.

Figure 11 shows the geometry of the homogeneous model for which analytic and numerical solutions were calculated. The first derivative of a Gaussian pulse is excited at the center of the model; numerical and analytic solutions are obtained at the three receivers shown in Figure 11. The numerical solutions were computed by the conventional and 25-point schemes. Figure 12 shows horizontal displacements at receiver 3. At receivers 1 and 2, there are no horizontal displacements [equation (34)]. Figure 13 shows vertical displacements at receivers 1, 2, and 3. In Figures 12 and 13, we can easily see some discrepancy between the exact solutions and the numerical solutions computed by the conventional second-order scheme, but the numerical solutions given by the 25-point scheme agree well with the exact solutions.

Computational efficiency

Previous second-order schemes use 9 grid points around the collocation to calculate solutions at a given node; the 25-point scheme uses 25 grid points. Although the operator

length of the 25-point scheme is larger than that of the previous second-order schemes, the scheme results in a smaller computational cost because it can reduce the number of grid points. For a 1% upper limit of error, the 25-point scheme reduces the total number of grid points to 10% of the conventional second-order scheme and to 37% of the combined second-order scheme (from dispersion analysis). The fewer grid points reduce computer memory requirements for storing the complex impedance matrix. The actual memory requirements are dependent on the method used to decompose the matrix. We will compute the storage amount required by a band-type matrix solver and a more sophisticated nested dissection matrix solver.

We will compare the storage amount of the 25-point scheme with those of the conventional and the combined second-order schemes [which Štekl and Pratt (1998) present]. Suppose that the number of grid points along the x-axis is the same as that along the z-axis. If the number of grid points required for the conventional scheme is $N \times N$ for a model, the number of grid points is $(3/11)N \times (3/11)N$ with 9 grid points per wavelength in the combined scheme and $(1/10)N \times (1/10)N$ with 3.3 grid points in the 25-point scheme to simulate a model of exactly the same size. All models are calculated such that the group velocity errors remain below 1%.

The storage amounts for the band-type matrix solver are shown in Table 1. Generally, the storage requirements for the nested dissection matrix solver are given by $C_2 N^2 \log_2 N + O(N^2)$ (George and Liu, 1981; Štekl and Pratt, 1998). Table 2 shows the storage requirements for the nested dissection method, obtained under the assumption that $O(N^2)$ can be neglected compared to $C_2 N^2 \log_2 N$.

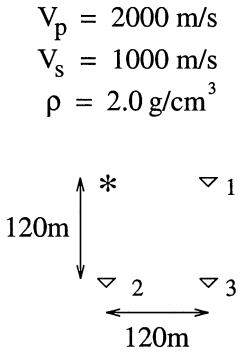

FIG. 11. The geometry of the homogeneous model.

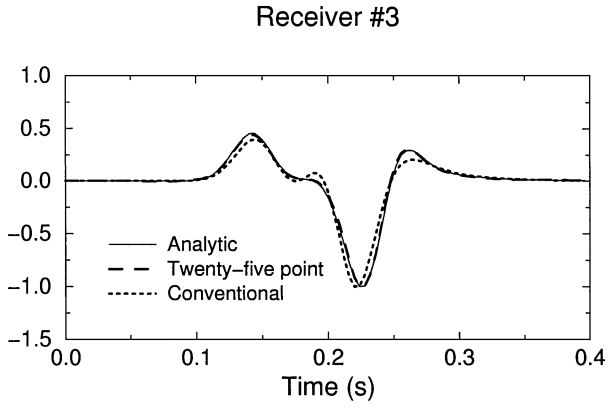

FIG. 12. Analytic solutions (solid line) and numerical solutions by the 25-point weighted-averaging scheme (dashed line) and the conventional finite-difference scheme (dotted line) for horizontal displacements at receiver 3 of Figure 11. The number of grid points per minimal shear wavelength is 3.3.

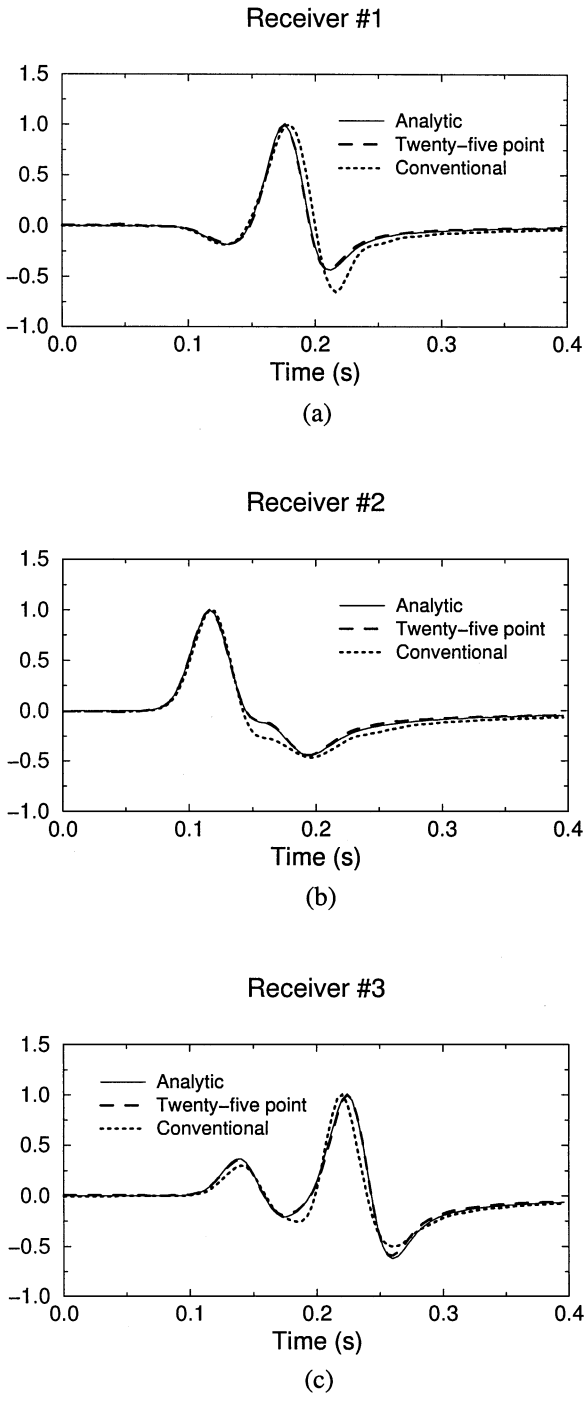

FIG. 13. Analytic solutions (solid line) and numerical solutions by the 25-point weighted-averaging scheme (dashed line) and by the conventional finite-difference scheme (dotted line) for vertical displacements at (a) receiver 1, (b) receiver 2, and (c) receiver 3 of Figure 11. The number of grid points per minimal shear wavelength is 3.3.

From Tables 1 and 2, we observe that the 25-point scheme achieves a 90% reduction with the band-type matrix solver and a 46% reduction with the nested dissection method in the computer memory requirements needed to store and factor the complex impedance matrix, compared with those for the combined scheme. We expect that the 25-point scheme will be more powerful for simulating a realistic model than other frequency-domain schemes and that the savings will be even greater when the analog of the proposed scheme is applied to 3-D elastic modeling.

Boundary conditions

We apply a stress-free condition at the free surface, written as

$$\frac{\partial u}{\partial z} + \frac{\partial v}{\partial x} = 0 \tag{36}$$

and

$$\frac{\lambda}{\rho}\frac{\partial u}{\partial x} + \frac{\lambda + 2\mu}{\rho}\frac{\partial v}{\partial z} = 0. \tag{37}$$

To discretize equations (36) and (37), we use a one-sided difference approximation for the vertical spatial derivative $(\partial/\partial z)$ and a central difference approximation for the horizontal derivative $(\partial/\partial x)$. For a grid point (i, j) at the free surface, we use grid points (i, j) and $(i, j+1)$ to approximate a vertical spatial derivative and use grid points $(i-1, j+1/2)$ and $(i+1, j+1/2)$ to approximate a horizontal derivative. We use the average of the displacements at $(i-1, j)$ and $(i-1, j+1)$ for the displacements at $(i-1, j+1/2)$ and use the average of the displacements at $(i+1, j)$ and $(i+1, j+1)$ for the displacements at $(i+1, j+1/2)$. These discretized conditions are expressed as

$$\frac{u_{i,j+1} - u_{i,j}}{\Delta z} + \frac{v_{i+1,j} + v_{i+1,j+1} - v_{i-1,j} - v_{i-1,j+1}}{4\Delta x} = 0 \tag{38}$$

Table 1. Storage requirements of the band-type matrix solver for the complex impedance matrix; C_1 is a constant.

	Storage amount	Percent improvement
Conventional scheme	$C_1 N^3$	100%
Combined scheme	$C_1 \left(\frac{3}{11}N\right)^3$	20%
25-point scheme	$2C_1 \left(\frac{1}{10}N\right)^3$	0.2%

Table 2. Storage requirements of the nested dissection matrix solver for the complex impedance matrix; C_2 is a constant.

	Storage amount	Percent improvement
Conventional scheme	$C_2 N^2 \log_2 N$	100%
Combined scheme	$C_2 \left(\frac{3}{11}N\right)^2 \log_2 \frac{3}{11}N$	7.4%
25-point scheme	$4C_2 \left(\frac{1}{10}N\right)^2 \log_2 \frac{1}{10}N$	4%

and

$$\frac{\lambda}{\rho}\left[\frac{u_{i+1,j} + u_{i+1,j+1} - u_{i-1,j} - u_{i-1,j+1}}{4\Delta x}\right] + \frac{\lambda + 2\mu}{\rho}\left[\frac{v_{i,j+1} - v_{i,j}}{\Delta z}\right] = 0. \tag{39}$$

To estimate the accuracy of the numerical solutions at the free surface boundary, we compare numerical solutions with analytic solutions for a semiinfinite medium (2-D Lamb problem). The analytic solutions are given by Ewing et al. (1957). Figures 14 and 15 show numerical and analytic solutions of horizontal and vertical displacements obtained at 300 and 450 m horizontally apart from the source for a homogeneous model whose compressional and shear wave velocities are 2000 and 1000 m/s, respectively, and density is 2.0 g/cm^3. The numerical solutions are compatible with the analytic solutions to some degree, but there exists some discrepancy. This discrepancy might result from using one-sided differencing operators for the vertical spatial derivatives and operators that are three points wide for the horizontal derivation. However, even when central differencing operators or 5-point-wide operators were used, we could not obtain better results. Furthermore, we note that the one-sided discretization operators for the stress-free condition make the complex impedance matrix unsymmetric, thereby violating the source-receiver reciprocity theorem. To obtain more accurate results, the finite-difference operators for the stress-free condition need to be studied further.

To suppress edge reflections resulting from finite-size modeling, we apply the sponge boundary condition of Shin (1995). This condition damps the wavefield gradually by defining damping coefficients which vary linearly from 1.0 to 0.9 within the sponge zone.

NUMERICAL EXAMPLES

We tested the 25-point scheme with a vertical-step model. The finite-difference scheme used here is a heterogeneous formulation of the 25-point scheme, obtained by considering variations of the elastic constants λ and μ and the density ρ from node to node in the manner of Kelly et al. (1976). We used the first derivative of a Gaussian pulse as the source.

Vertical-step model

The geometry of a vertical-step model is shown in Figure 16; the material properties are in Table 3. The explosive source, excited at a depth of 150 m, produces a source wavelet with a maximum frequency of 40 Hz. The receivers are spread on the surface. The spatial grid spacings are $\Delta x = \Delta z = 7.5$ m, and the numbers of spatial grid points for horizontal and vertical direction are $N_x = N_z = 201$. We applied stress-free conditions at the free surface boundary.

Figure 17 shows synthetic seismograms of horizontal and vertical displacements. The direct P-waves, which appear at

Table 3. Physical properties of the vertical-step model of Figure 16.

Layer	V_p	V_s	ρ
1	1700 m/s	1000 m/s	2.0 g/cm^3
2	2500 m/s	1470 m/s	2.4 g/cm^3
3	4000 m/s	2200 m/s	2.7 g/cm^3

$t = 0.0706$ s with reference to zero offset, are followed by Rayleigh waves. The Rayleigh waves have strong and constant amplitudes, even at the far offset. The *PP*-reflections from the first reflector appear at $t = 0.4$ s, and the *PS*- and *SP*-reflections resulting from mode conversion appear at $t = 0.56$ s and 0.515 s. The *SS*-reflections appear at 0.68 s for zero offset. At a later time, the reflections from the second reflector are corrupted by multiples. In the seismograms, the unwanted seismic waves which can be generated from artificial boundaries are effectively removed by the sponge boundary condition.

CONCLUSION

We have presented a 25-point weighted-averaging scheme that can be applied to elastic wave equations in the frequency domain. The 25-point scheme uses 25 grid points to approximate the second-order partial derivatives of displacements and the mass accelerations. This scheme allows us to reduce the number of grid points per shear wavelength necessary to achieve accurate results. Although we use a larger operator than other methods, the operator is accurate enough to reduce the overall computer memory requirements for the storage of the factored complex impedance matrix.

Our numerical dispersion analysis showed that the 25-point scheme requires 3.3 grid points per shear wavelength to achieve a 1% upper error limit in phase and group velocities. With the reduction in the number of grid points, the computer memory can be reduced by 90% for the band-type solver and 46% for the nested dissection method, respectively, relative to the combined second-order scheme suggested by Štekl and Pratt (1998). This reduction in computer memory enables the simulation of realistic models or the computation of high-frequency

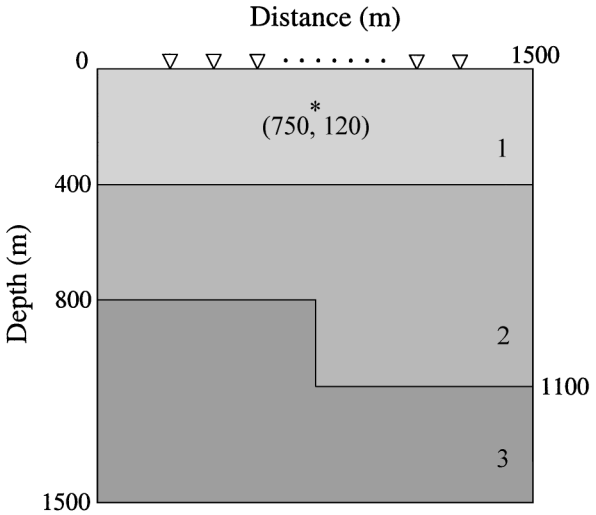

FIG. 16. The geometry of the vertical-step model.

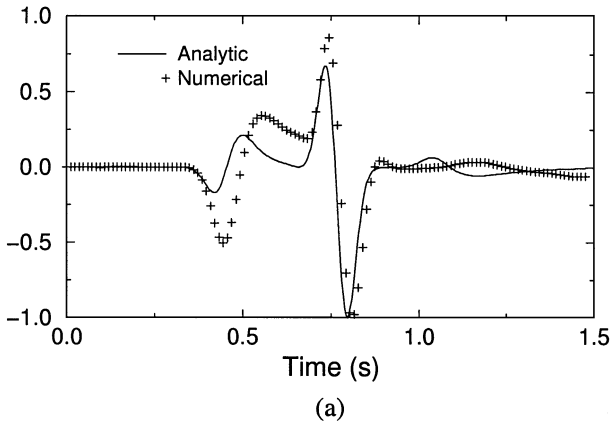

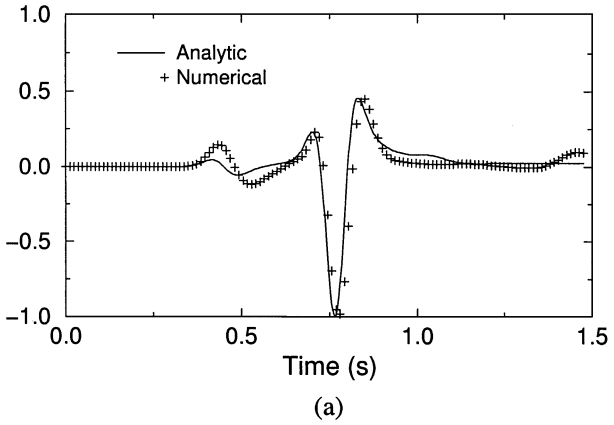

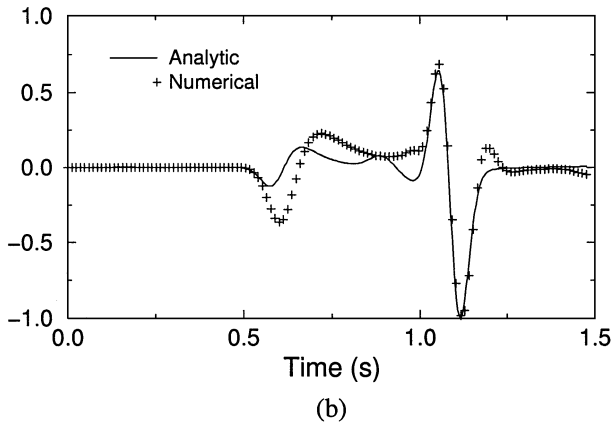

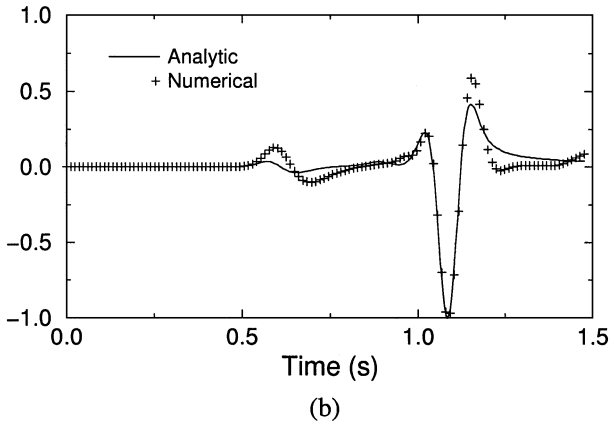

FIGS. 14, 15. Analytic (solid line) and numerical horizontal (Figure 14, left) and vertical (Figure 15, right) solutions obtained by the 25-point weighted-averaging scheme (plus symbol) for a 2-D Lamb problem for source–receiver offsets of (a) 300 m and (b) 450 m.

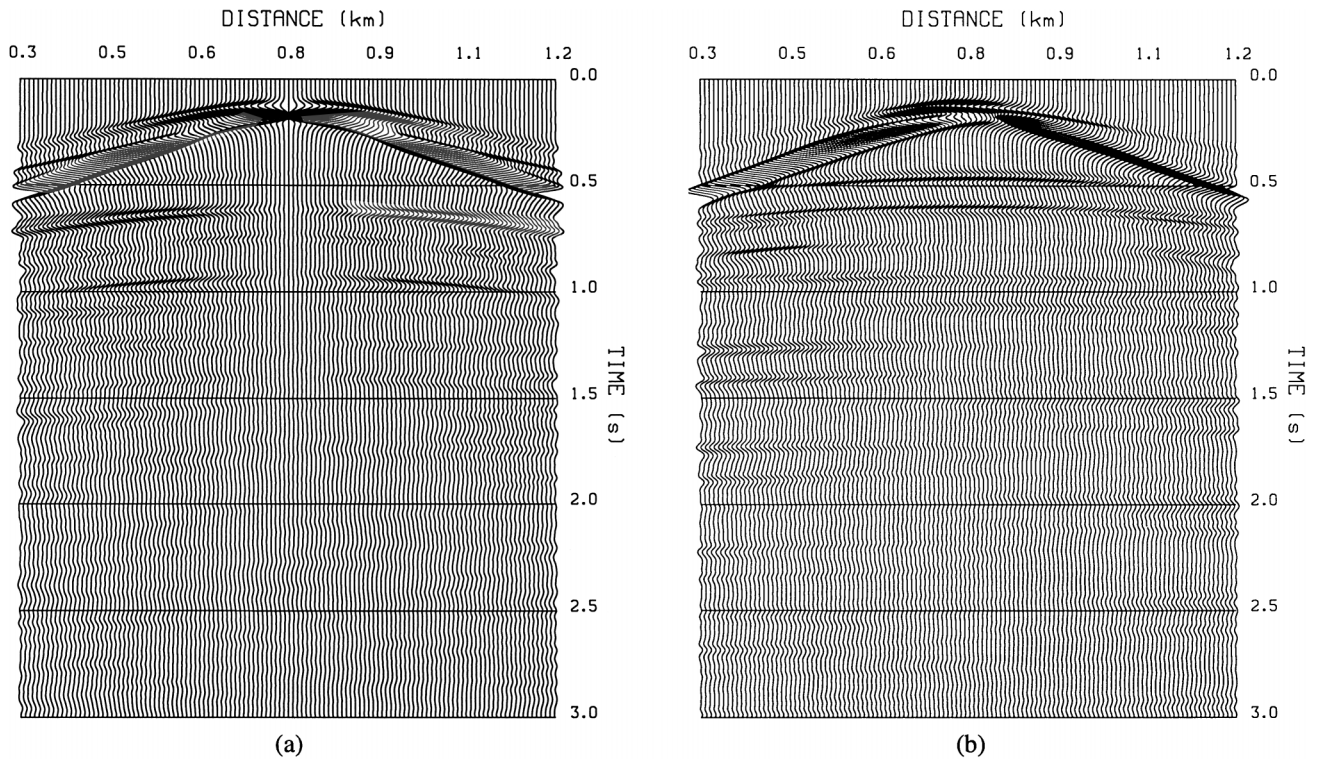

FIG. 17. Synthetic seismograms for the vertical-step model, observed on the surface: (a) horizontal motion, (b) vertical motion.

solutions. By comparing numerical solutions with analytic solutions for an infinite homogeneous model, we found that the 25-point scheme matches the exact solution. In addition, we successfully generated synthetic seismograms for a vertical-step model using the 25-point scheme. However, our 25-point scheme does not yield an exact solution for the 2-D Lamb problem. We need to study further the method of discretizing the stress-free condition to improve the accuracy of the 25-point scheme for the 2-D Lamb problem.

We expect that our 25-point scheme can be applied to prestack elastic migration and to AVO analysis at large offsets, which require simulation of large-size models.

REFERENCES

Eason, G., Fulton, J., and Sneddon, I. N., 1956, The generation of waves in an infinite elastic solid by variable body forces: Phil. Trans. Roy. Soc., London, **A 248**, 575–607.

Ewing, W. M., Jardetzky, W. S., and Press, F., 1957, Elastic waves in layered media: McGraw-Hill Book Co.

George, A., and Liu, J. W., 1981, Computer solution of large sparse positive definite systems: Prentice-Hall, Inc.

Jo, C. H., Shin, C., and Suh, J. H., 1996, An optimal 9-point, finite-difference, frequency-space, 2-D scalar wave extrapolator: Geophysics, **61**, 529–537.

Kelly, K. R., Ward, R. W., Treitel, S., and Alford, R. M., 1976, Synthetic seismograms: A finite-difference approach: Geophysics, **41**, 2–27.

Lines, L. R., and Treitel, S., 1984, A review of least-squares inversion and its application to geophysical problems: Geophys. Prosp. **32**, 159–186.

Lysmer, J., and Drake, L. A., 1972, A finite-element method for seismology, *in* Bolt, B. A., Ed., Methods in computational physics, vol. **11**: Seismology: Surface waves and earth oscillations: Academic Press, Inc.

Marfurt, K. J., 1984, Accuracy of finite-difference and finite-element modeling of the scalar and elastic wave equations: Geophysics, **49**, 533–549.

Marfurt, K. J., and Shin, C., 1989, The future of iterative modeling in geophysical exploration, *in* Eisner, E., Ed., Handbook of geophysical exploration: **I**—Seismic Exploration, Vol. **21**: Supercomputers in seismic exploration: Pergamon Press, 203–228.

Pilant, W. L., 1979, Elastic waves in the earth: Elsevier Science Publ. Co., Inc.

Pratt, R. G., 1990a, Inverse theory applied to multi-source cross-hole tomography, part **II**: Elastic wave-equation method: Geophys. Prosp., **38**, 287–310.

———1990b, Frequency-domain elastic wave modeling by finite differences: A tool for crosshole seismic imaging: Geophysics, **55**, 626–632.

Pratt, R. G., and Worthington, M. H., 1990, Inverse theory applied to multi-source cross-hole tomography, **I**: Acoustic wave-equation method: Geophys. Prosp., **38**, 287–310.

Shin, C., 1988, Nonlinear elastic wave inversion by blocky parameterization: Ph.D. thesis, Univ. of Tulsa.

———1995, Sponge boundary condition for frequency-domain modeling: Geophysics, **60**, 1870–1874.

Shin, C., and Sohn, H., 1998, A frequency-space 2-D scalar wave extrapolator using extended 25-point finite-difference operators: Geophysics, **63**, 289–296.

Štekl, I., and Pratt, R. G., 1998, Accurate viscoelastic modeling by frequency-domain finite differences using rotated operators: Geophysics, **63**, 1779–1794.